information services
gwasanaethau gwybodaeth

Catalytic oxidation of 1,2-dichloroethane over three-dimensional ordered meso-macroporous Co_3O_4/$La_{0.7}Sr_{0.3}Fe_{0.5}Co_{0.5}O_3$: Destruction route and mechanism

Mingjiao Tian[a], Chi He[a,b], Yanke Yu[a], Hua Pan[c], Louise Smith[b], Zeyu Jiang[a], Ningbo Gao[a], Yanfei Jian[a], Zhengping Hao[d], Qing Zhu[a]

[a] Department of Environmental Science and Engineering, State Key Laboratory of Multiphase Flow in Power Engineering, School of Energy and Power Engineering, Xi'an Jiaotong University, Xi'an, 710049, Shaanxi, P.R. China
[b] Cardiff Catalysis Institute, School of Chemistry, Cardiff University, Main Building, Park Place, Cardiff, CF10 3AT, UK
[c] College of Biology and Environmental Engineering, Zhejiang Shuren University, Hangzhou, 310015, Zhejiang, P.R. China
[d] Department of Environmental Nano-Materials, Research Center for Eco-Environmental Sciences, Chinese Academy of Sciences, Beijing, 100085, P.R. China

ARTICLE INFO

ABSTRACT

Three-dimensional ordered meso-macroporous $La_{0.7}Sr_{0.3}Fe_{0.5}Co_{0.5}O_3$ (3DOM LSFCO)-supported Co_3O_4 catalysts were designed and prepared via a PMMA-templating strategy for the total oxidation of 1,2-dichloroethane (1,2-DCE). The physicochemical properties of all synthesized samples were characterized by XRD, FE-SEM, TEM, HAADF-STEM, low-temperature N_2 sorption, XPS, H_2-TPR, and in situ FT-IR. The introduction of Co_3O_4 increases the generation rate of oxygen vacancy, playing a crucial role in adsorption and activation of oxygen species. The special 3DOM structure of perovskite-type oxide promotes 1,2-DCE molecules to effectively and intimately contact with the surface adsorbed oxygen over supported catalysts and further accelerates the redox process. Compared with pure LSFCO, all the Co_3O_4 supported catalysts show superior catalytic performance with reaction rate increases from 5.53×10^{-12} to 2.29×10^{-11} mol g^{-1} s^{-1} and E_a decreases from 74.7 to 22.6 KJ mol^{-1}. Amongst, the $10Co_3O_4$/3DOM LSFCO catalyst exhibits the best catalytic activity, highest resistance to chlorine poisoning and lowest by-products concentration because of the largest amount of surface adsorbed oxygen. CO_2, CO, HCl, and Cl_2 are the main oxidation productions, while some typical reaction intermediates such as vinyl chloride, 1,1,2-trichloroethane and trichloroethylene are also observed, especially over the 3DOM LSFCO sample. Furthermore, the reaction mechanism of 1,2-DCE oxidation over obtained catalysts was proposed based on the results of gas chromatography, in situ FT-IR, and on-line MS. It is believed that the Co_3O_4/3DOM LSFCO are promising catalysts for the total removal of chlorinated volatile organic compounds.

1. Introduction

Chlorinated volatile organic compounds (CVOCs) emitted to atmo-sphere can result in serious impact on human health and the environ-ment due to their distinct toxicity, high stability and persistence [1,2]. 1,2-dichloroethane (1,2-DCE), regarded as a representative member of CVOCs, is widely used in different manufacturing processes such as industrial solvent and metal degreaser [3], making great contributions to the ozone layer depletion, photochemical smog and haze [4]. Various control methods, such as adsorption, absorption [5], catalytic oxidation [6] and pyrolysis [7], have been exploited to solve this problem, among which catalytic oxidation is considered to be one of the most promising

candidates for CVOCs total elimination ascribed to its high activity, controllable selectivity, and low energy consumption [8].

Different types of noble metal-based catalysts with satisfied activity have been developed for CVOCs destruction in recent years, but the high cost and inferior resistance to heteroatom poisoning and thermal stability greatly limited their vast application [9–11]. Besides, the low boiling point of noble metal nanoparticles which are prone to aggregate and even evaporation under elevated temperatures also restricts their application under practical conditions [12]. Comparatively, transitional metal oxides possess advantages of low cost, abundant regulatory space, excellent reducibility and thermal stability, and superior chlorine resistance, endowing them as one kind of potential and promising
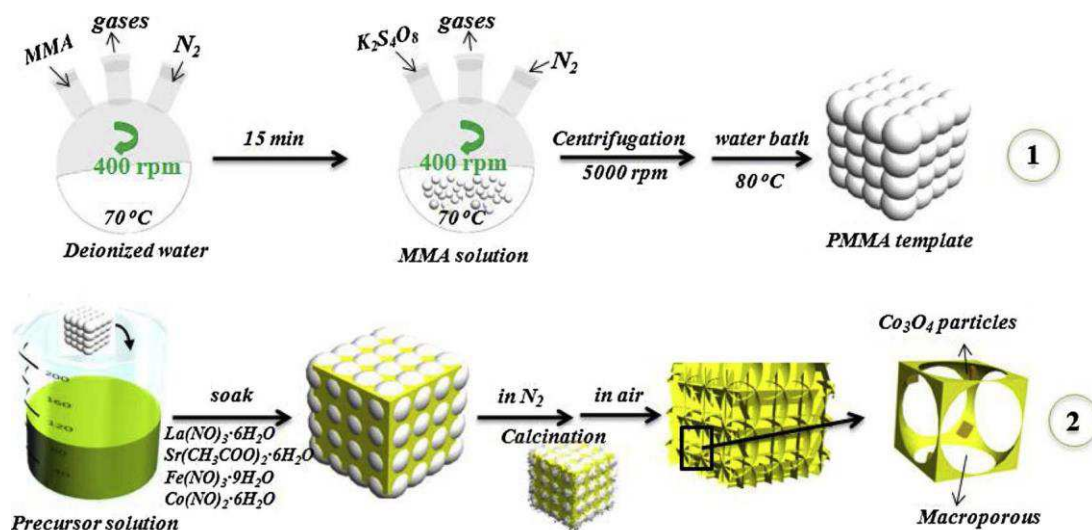
Scheme 1. Schematic illustration for the preparation of three-dimensional ordered meso-macroporous catalyst.

materials for CVOCs removal [13–16]. However, the inferior low-temperature activity and chlorine resistant of conventional transitional metal oxides is an enormous obstacle for their practical applications. Therefore, the development of good stability and highly efficient transitional metal oxide-based catalysts for CVOCs total elimination is of great importance.

ABO3 perovskites with excellent structure stability caught in-vestigators' eyes for the oxidation of VOCs recently. In the structure of perovskite, the A cation, which usually is lanthanum (La), has a do-decahedral coordination, and the B cation with a six-fold coordination can often be a transition metal to control the reduction and oxidation reactions [17], which suggests that substitution of B cation is crucial to the combustion of CVOCs. Many studies suggest that La substituted by Sr in A cation can improve activity and stability of the perovskite ma-terial [18]. Simultaneously, the elements selectivity of B cation favors the formation of highly active oxygen species. At present, perovskite-type oxides are widely studied in catalytic oxidation field. However, very few works has focused on the catalytic oxidation of CVOCs over perovskite-type oxides, primarily due to the unsatisfied activity at low temperature, which is related to the limited surface areas and se-lectivity of the elements. In fact, the industrial reaction temperatures are obviously higher than those used in the lab-scaled tests. For ex-ample, the catalyst bed temperatures in the most adopted industrial regenerative catalytic oxidizer (RCO) are generally much higher than 300 °C. Moreover, the formation of steam under high temperature during CVOCs oxidation can lessen the chlorine poison by taking the chlorinated species away from catalyst surface [19]. Consequently, the good thermal stability and chlorine resistance should be highly con-cerned for designing the CVOC oxidation materials. The good structure stability of perovskite-type oxides are worth to be considered and ex-plored in CVOCs catalytic oxidation. Meanwhile, the surface area and the porosity of perovskite-type oxides can be modified by using novel preparation techniques instead of the traditional preparation methods such as the sol-gel [20–22] and ball-milling protocols [23,24]. The polymethyl methacrylate (PMMA)-templating method [25–27] are evidenced as an efficient route to synthesis porous oxides with three-dimensional ordered meso-macroporous (3DOM) structures that can improve the transportation and diffusion properties of the gas phase molecules. Additionally, the introduction of certain amounts of active capping agent to metal oxides can produce mesopores and further en-hance the surface area [26]. Fe and Co-based perovskite-type oxides are widely studied for the outstanding thermal stability and high oxidation activity in the catalytic oxidation filed [28]. And it is reported that the Co3O4 is an environment-friendly and highly active oxide for VOC

oxidation [29,30].

In this work, the advantages of Co3O4 and 3DOM perovskite-type oxide were innovatively combined with the target to develop more active catalysts. A series of 3DOM LSFCO supported Co3O4 (5−16 wt.%) catalysts were synthesized by the PMMA-templating strategy, and their physicochemical properties and catalytic behaviors in the total oxida-tion of 1,2-DCE were systematically investigated. The selectivity of primary products (i.e., CO, CO2, Cl2, and HCl), distribution of reaction intermediates, and chlorine poisoning and high-temperature stability of the prepared samples were also studied. Furthermore, the oxidation route and mechanism of 1,2-DCE over Co3O4/3DOM LSFCO were also clarified. We believe that the obtained Co3O4/3DOM La0.7Sr0.3Fe0.5Co0.5O3 catalyst should be a promising and powerful candidate for CVOCs oxidation.

2. Experimental

2.1. Preparation of PMMA microspheres

The well-arrayed PMMA microspheres were firstly synthesized by the following procedures. Typically, 650 mL of deionized water was added into a three-necked flask and heated at 70 °C under a medium stirring speed for 30 min, which was degassed with continuous flowing N_2 of 250 mL min^{-1}, causing an oxygen-free environment. And then, 55 mL of methyl methacrylate with 0.016 g p-hydroxybenzonic acid was poured into the deionized water with temperature maintained at 70 °C. After 15 min, 0.2 g of $K_2S_4O_8$ was mixed with the above solution and maintained at 70 °C for 40 min until a white homogeneous sus-pension was obtained, which was poured into 2000 mL of deionized water immediately. The diluted white mixture was centrifuged for 50 min at 5000 rpm. The recovered material was washed with deio-nized water, and the resulting precipitate was dried in a water bath at 80 °C for 5 h until a well-arrayed PMMA template was obtained, as exhibited in Scheme Scheme 1.

2.2. Preparation of Co3O4/3DOM La0.7Sr0.3Fe0.5Co0.5O3 catalysts

Co3O4/3DOM La0.7Sr0.3Fe0.5Co0.5O3 catalysts were prepared by an in situ synthesis with the PMMA-templating strategy using the pre-synthesized well-arrayed PMMA microsphere as the hard template. In a typical procedure, stoichiometric amounts of La(NO)3·6H2O, Sr (CH3COO)2·6H2O, Fe(NO)3·9H2O and Co(NO)2·6H2O were dissolved in 7 mL of ethylene glycol (EG) at room temperature under vigorous stirring for 4.5 h until the formation of a transparent solution. Then,

1.5 g of polyethylene oxide–polypropylene oxide–polyethylene oxide (PEO-PPO-PEO, P123) was dissolved in 7 mL of methanol, which was mixed with the metal nitrate-containing transparent solution under stirring for 1 h. After that, about 2.0 g of PMMA hard template was soaked in the precursor solution for 6 h. After filtering the excessive liquid, the solid was dried at room temperature. The resulting solid was calcined at 300 °C for 3 h under a N_2 flow of 250 mL min^{-1} (heating rate of 1 °C min^{-1}), followed by heating up to 650 °C with the same heating rate with air atmosphere. Finally, the $yCo_3O_4/3DOM$ LSFCO catalysts with various Co_3O_4 loadings (y = 5–16 wt.%) were obtained, as exhibited in Scheme Scheme 1.

2.3. Catalytic activity tests

Catalytic oxidation of 1,2-dichloroethane was evaluated in a continuous flow quartz tube reactor (I.D. = 10 mm), in which the temperature is controlled with a K-type thermocouple placed in the catalyst bed. 0.5 g of synthesized catalyst (40–60 mesh) and 500 ppm of 1,2-DCE in 400 mL min^{-1} of air stream (21 vol.% O_2, N_2 balance) with a gas hourly space velocity (GHSV) of 48,000 h^{-1} were used in each test. Catalytic activity was measured in the temperature range of 200–580 °C, and the 1,2-DCE conversion was calculated by the difference between inlet and outlet 1,2-DCE concentrations. The reactants, reaction products (CO, CO_2, HCl and Cl_2) and chlorinated by-products were analyzed by an on-line ECD gas chromatograph (GC9890) equipped with ECD and FID detectors and an on-line mass spectroscopy (MS, SHP8400 PMS-L). In addition, the concentrations of HCl and Cl_2 were also tested and adjusted by the on-line HCl and Cl_2 detectors. The following equations were used to calculate the conversion of 1,2-DCE as well as the CO, CO_2, HCl, and Cl_2 selectivity:

$$1,2\text{-DCE conversion (\%)} = \frac{[1,2\text{-DCE}]_{in} - [1,2\text{-DCE}]_{out}}{[1,2\text{-DCE}]_{in}} \times 100 \tag{1}$$

$$\text{CO selectivity (\%)} = \frac{[CO]}{[CO] + [CO_2] + x[C_x H_y Cl_z]} \times 100 \tag{2}$$

$$CO_2 \text{selectivity(\%)} = \frac{[CO_2]}{[CO] + [CO_2] + x[C_x H_y Cl_z]} \times 100 \tag{3}$$

$$Cl_2 \text{ selectivity(\%)} = \frac{2[Cl_2]}{[HCl] + 2[Cl_2] + z[C_x H_y Cl_z]} \times 100 \tag{4}$$

$$\text{HCl selectivity(\%)} = \frac{[HCl]}{[HCl] + 2[Cl_2] + z[C_x H_y Cl_z]} \times 100 \tag{5}$$

where $[1,2-DCE]_{in}$ and $[1,2-DCE]_{out}$ are the inlet and outlet con-centrations of 1,2-DCE, respectively. $C_xH_yCl_z$ is corresponded to the chlorinated by-products that result from the incomplete combustion of the feed 1,2-DCE (all concentrations are in ppm).

2.4. Catalyst characterizations

The morphology and microstructure of the samples were observed using a JEOL JSM-7800F field-emission scanning electron microscope (FE-SEM) and a JEOL 1200CX transmission electron microscope (TEM) equipped with an OXFORDMAX-80 energy-dispersive X-ray detector (EDS) for elemental analysis.

X-ray diffraction (XRD) patterns were performed at room tempera-ture on a PANalytical X'pert MPD Pro X-ray diffractometer with Cu Kα radiation (λ = 1.5418 Å). The X-ray tube was operated at 40 kV and 40 mA. The diffractograms were recorded in the 2θ range of 10–80 °C with a 2θ step size of 0.01° and a counting time of 10 s per step.

Nitrogen adsorption-desorption isotherms were carried at −196 °C on a Builder SSA-6000 automatic gas sorption analyzer. All samples were pretreated at 300 °C under vacuum for 4 h. The specific surface area (S_{BET}) was calculated using the Brunauer–Emmet–Teller (BET) method using the linear part of BET plots, and the pore size distribution

was derived from the adsorption branch of the N_2 isotherm using the Barrett−Joyner−Halenda (BJH) method. The total pore volume (D_V) was estimated form the amount of N_2 adsorbed at a relative pressure (P/P_0) of ca. 0.99.

The chemical compositions of the samples were carried on a Kratos Axis Ultra DLD multifunctional X-ray photoelectron spectrometer (XPS). Binding energies (BE) were calibrated relative to the C 1s peak (284.8 eV) from adventitious carbon adsorbed on the surface of the samples.

The reducibility of all samples were examined by the hydrogen temperature programmed reduction (H_2-TPR) on a PCA-1200 analyzer. The catalyst (100 mg) was pretreated at 400 °C for 30 min in the presence of Ar with the flow of 40 mL min^{-1} to remove the adsorbed CO_2 and H_2O before H_2-TPR test. When cooled to room temperature, the catalyst was treated in 5% H_2/Ar with the flow of 30 mL min^{-1} from 50 to 900 °C with a heating rate of 10 °C min^{-1}. The alteration in H_2 concentration of the outlet gases was monitored on-line by the thermal conductivity detector (TCD) and the reduction band was calibrated against that of the complete reduction of a standard CuO sample (Ourchem, 99.99%).

Temperature programmed desorption of O_2 (O_2-TPD) was performed on the same equipment as H_2-TPR. 100 mg of catalyst was pretreated in N_2 flow (30 mL/min) at 400 °C for 1 h and then cooled to room temperature prior to adsorption of O_2 for 30 min. After being saturated with O_2, the catalyst was flushed with pure N_2 flow (30 mL/min) for 1 h at room temperature. The desorption profiles of O_2-TPD were recorded online at a heating rate of 10 °C/min from 30 to 900 °C.

The adsorption of 1,2-DCE was examined by the in situ infrared spectroscopy (DRIFTS), which was carried out using a Bruker Tensor37 FT-IR equipped with a controlled-temperature and environment diffusive reflectance chamber with KBr windows and an MCT detector cooled by liquid nitrogen. The sample (50 mg) was pretreated at 500 °C for 1 h in a flow of N_2 (40 mL min^{-1}) and then cooled down to 100 °C to collect the background spectrum. Then, the adsorption spectra were collected for 90 min at 100 °C in the presence of 500 ppm of 1,2-DCE. All the spectra were collected in range of 4000–800 cm^{-1} with 100 scans at an instrument resolution of 4 cm^{-1}.

3. Results and discussion

3.1. Structural and textural properties

The crystal properties of the synthesized samples were characterized by XRD, and the diffraction patterns are shown in Fig. 1A. The obtained samples exhibit obvious diffraction peaks at 2θ of 23.0°, 32.8°, 40.4°, 47.0°, 58.5°, 68.7°, suggesting the formation of orthorhombic ABO_3 phase, which is in good agreement with the standard $La_{0.7}Sr_{0.3}Fe_{0.5}Co_{0.5}O_3$ sample (JCPDS No. 01-089-1267). A small dif-fraction peak centered at 2θ = 36.7° can be observed over all 3DOM LSFCO supported cobalt catalysts, assigning to the Co_3O_4 (311) lattice plane of cubic Co_3O_4 (JCPDS No. 01-074-2120). As shown in Fig. 1B, the intensity of Co_3O_4 diffraction peaks increases continuously with the increasing of cobalt loading amount from 5 to 16 wt.%, which suggests the partial aggregation of surface Co_3O_4 phase. As shown in Fig. S1 (Supplementary Material, SM), two characteristic bands at 590 and 426 cm^{-1} over the fresh samples can be attributed to the stretching and bending vibration of CoeO bonds in LSFCO. Another peak appeared at 668 cm^{-1} can be assigned to the vibration of CoeO bonds in the Co_3O_4 structure. No bond vibration corresponding to CeC or CeH can be observed, indicating that all organic molecules used for catalyst synthesis are totally removed by the thermal treatment [25].

The typical formation scheme of the PMMA template and Co_3O_4/ 3DoM $La_{0.7}Sr_{0.3}Fe_{0.5}Co_{0.5}O_3$ catalysts is depicted in Scheme Scheme 1. PMMA microspheres are synthesized by copolymerization of MMA and p-hydroxybenzonic acid using suitable initiators in N_2 atmosphere, with the latex centrifuged and dried to result in the highly ordered PMMA
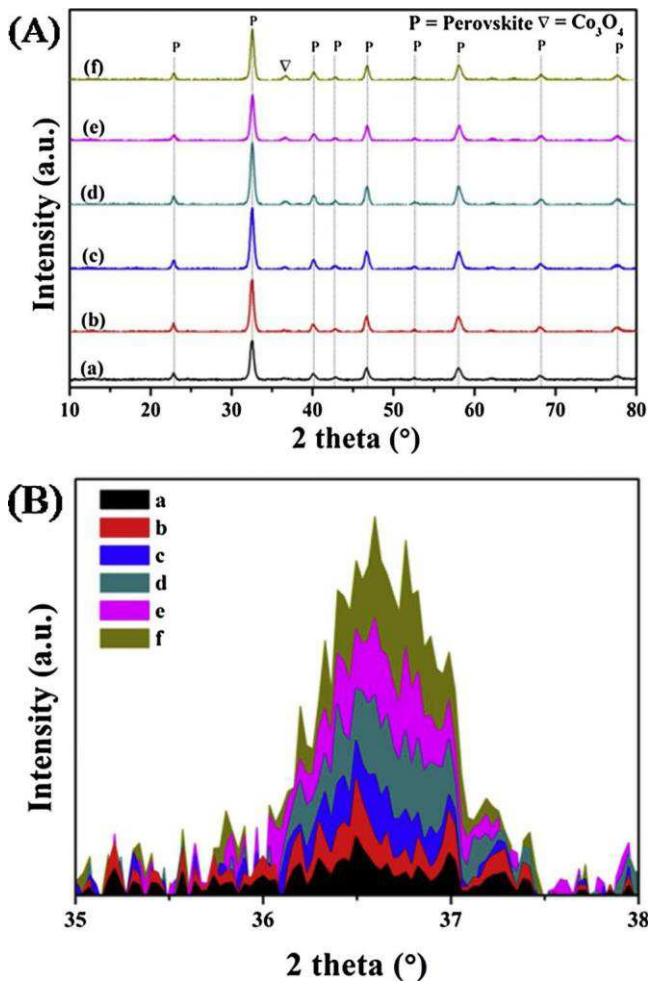
Fig. 1. (A) XRD patterns and (B) corresponding Co_3O_4 XRD plots of (a) 3DOM LSFCO, (b) $5Co_3O_4$/3DOM LSFCO, (c) $8Co_3O_4$/3DOM LSFCO, (d) $10Co_3O_4$/3DOM LSFCO, (e) $12Co_3O_4$/3DOM LSFCO, and (f) $16Co_3O_4$/3DOM LSFCO.

materials. The mixture of metal precursor dissolved in the capping agent of EG and P123 was soaked in the highly ordered organic tem-plate, and then the organics layer removed by pyrolysis at 650 °C to obtain a 3DOM oxide structure. Fig. 2 shows typical SEM images of synthesized catalyssts. Highly ordered PMMA microsphere hard tem-plate with an average diameter of about 300 nm can be found in Fig. 2a–c. It can be observed that the LSFCO sample displays a 3DOM microstructure with an average macropore size of around 130 nm, which corresponded to a large shrinkage following removal of the PMMA microspheres, compared to the initial size of PMMA micro-spheres. Typically, the shrinkage is caused by the melting of the polymer templates and the sintering of the produced metal oxides. However, the uniform pore structure of prepared samples is not de-stroyed by this enormous shrinkage [31]. Besides, the 3DOM structure of LSFCO is not affected after loading of different amounts of Co_3O_4.

The 3DOM structure of samples were further demonstrated by TEM patterns (Fig. 3a–p). The macroporous structure is in agreement with the results obtained by the SEM results. And the formation of LSFCO perovskite phase is also verified by the HR-TEM result (Fig. 3b) because the d value of the (112) crystal planeis estimated to be 0.271–0.272 nm corresponding to the standard orthorhombic $La_{0.7}Sr_{0.3}Fe_{0.5}Co_{0.5}O_3$ (JCPDS No. 01-089-1267) identified by the XRD measurement. The d value of the (311) crystal plane of Co_3O_4 in $10Co_3O_4$/3DOM LSFCO is also confirmed (ca. 0.242 nm) in Fig. 3d according to the standard cubic Co_3O_4 oxide (JCPDS No. 01-074-2120). It's worth to mention that the face center cubic (112) plane of 3DOM LSFCO and the (311) crystal

plane of Co_3O_4 have a contact angle of about 90°, indicating the ex-istence of a strong interaction between Co_3O_4 and 3DOM LSFCO, which can be associated with the improvement of the catalytic activity. The silicon drift detector (SDD) energy dispersive spectrometry (EDS) was also used to evaluate the integrated intensity of La, Sr, Fe, Co, and O elements of 3DOM LSFCO (Fig. 3f–j) and $10Co_3O_4$/3DOM LSFCO (Fig. 3l–p), and the result reveals that all test elements are homo-geneously distributed.

The N_2 adsorption-desorption isotherms and pore size distribution of the 3DOM LSFCO and yCo_3O_4/3DOM LSFCO samples are shown in Fig. 4. All synthesized samples present a type II isotherm (Fig. 4A). The portion of the low-pressure almost presents a linear middle section of the isotherm attributing to multilayer adsorption and thereby demon-strating that the samples are nonporous or macroporous adsorbents [31]. With increasing of the relative pressure (P/P_0), capillary con-densation appears and all the samples display H3 hysteresis loops in P/P_0 range of 0.9−1.0, attesting the existence of mesopores in the catalysts [32]. In addition, the different size of the hysteresis loops between the yCo_3O_4/3DOM LSFCO and 3DOM LSFCO catalysts demonstrates the modification of Co_3O_4 for the 3DOM LSFCO. Fig. 4B shows that there is an obvious peak at pore diameter between of 2 and 10 nm, indicating the presence of large amounts of mesopores inside the macropore walls of the samples. Amongst, the $10Co_3O_4$/3DOM LSFCO exhibits the highest peak at pore diameter of 2−10 nm (centered at 2.61 nm), sug-gesting the existence of the most abundant of mesopores. Although the $8Co_3O_4$/3DOM LSFCO sample also owns a very high mesoporous peak (centered at 2.54 nm), its pore size distribution is much wider than other samples, indicating the non-uniform mesoporous distribution. Therefore, the meso-macroporous hybrid structure of synthesized cat-alysts can be confirmed by combining the characterization results of SEM, TEM and low-temperature N_2 sorption (Figs. 2–4). Macroporous skeleton of the samples accelerates the mass transfer of 1,2-DCE mo-lecules and inner mesopores further promote the reactants to reach and contact with the active sites over the catalyst. The BET surface areas (11.9−17.7 m^2 g^{-1}) of the 3DOM samples are higher than that of the pervoskite using methods of solid state reaction of the oxides, copre-

cipitation of the nitrates, wet ball-milling and citrate complexation (< 10 m^2 g^{-1}) [33,34].

3.2. Surface composition and element status

XPS analysis was performed to give an insight into chemical state of La 3d, Sr 3d, Fe 2p, Co 2p, and O 1s (deconvoluted by fitting a Gaussian-Lorentzian (GL) function with a Shirley background) over the prepared catalysts, as shown in Fig. 5 and Fig. S2B. Two peaks assigned to La $3d_{5/2}$ at BE of 833.7 and 837.6 eV and the peaks at BE of 850.3 and 854.9 eV corresponding to La $3d_{3/2}$ are associated with the La^{3+} ion in the perovskite (Fig. 5A) [32,35,36].

Fe 2p XPS spectra (Fig. 5B) consist of Fe $2p_{3/2}$ (BE = 710.0 eV) and Fe $2p_{1/2}$(BE = 723.8 eV) with the spin orbit separation of 13.8 eV [37]. Fe $2p_{3/2}$ peak can be further deconvoluted into two sub-peaks centered at 710.3 and 713.3 eV, corresponding to the Fe^{2+} and Fe^{3+}, respec-tively [38,39]. The ratios of Fe^{3+}/Fe^{2+} over all prepared samples are shown in Table S1 (SM). Co $2p_{3/2}$ and Co $2p_{1/2}$ peaks featured at the binding energies of 779.7 eV and 795.1 eV with the separation of the binding energy of 15.4 eV can be observed in the Co 2p spectra (Fig. 5C), confirming the presence of the Co_3O_4 spinel phase [16]. Hence, the Co_3O_4 is regarded as the main surface cobalt phase in the catalysts, in accordance with the XRD results (Fig. 1A). Meanwhile, the satellite peaks located at 786.3 and 803.0 eV can be attributed to the octahedral symmetry CoO [40]. To learn more about the cobalt che-mical state over the samples, Co $2p_{3/2}$ and Co $2p_{1/2}$ are further de-convoluted into two sub-peaks, respectively. The Co $2p_{3/2}$ peak at 779.8 eV and the Co $2p_{1/2}$ peak at 794.8 eV with the spin-orbit splitting dif-ference of 15.0 eV can be assigned to the octahedral Co^{3+}, and the Co $2p_{3/2}$ peak at 781.3 eV and the Co $2p_{3/2}$ peak at 796.1 eV are in
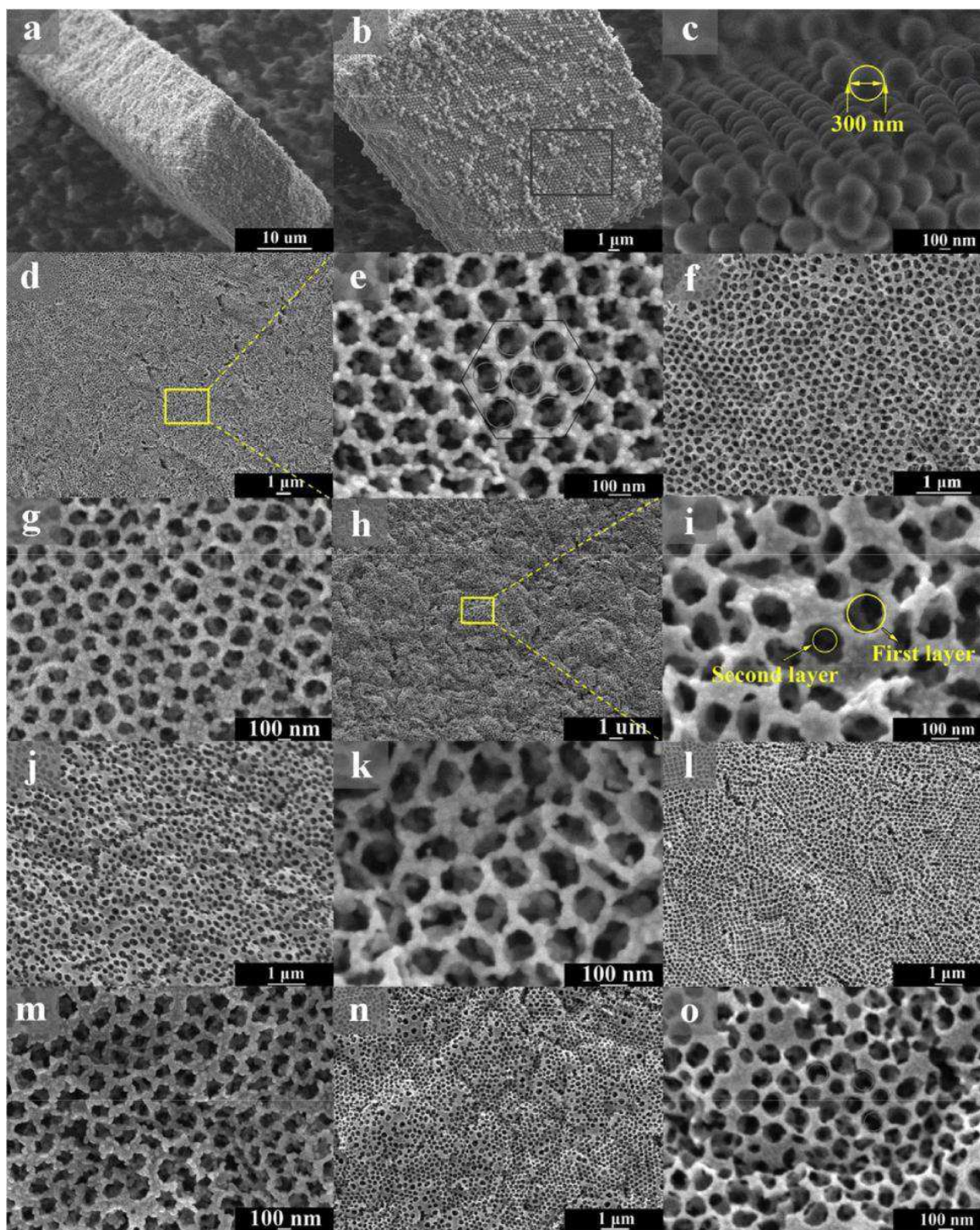
Fig. 2. Typical FE-SEM images of (a–c) PMMA microsphere, (d and e) 3DOM LSFCO, (f and g) 5Co$_3$O$_4$/3DOM LSFCO, (h and i) 8Co$_3$O$_4$/3DOM LSFCO, (j and k) 10Co$_3$O$_4$/3DOM LSFCO, (l and m) 12Co$_3$O$_4$/3DOM LSFCO, and (n and o) 16Co$_3$O$_4$/3DOM LSFCO.

accord with the existence of tetrahedral Co^{2+} [41]. The proportion of Co^{3+}/Co^{2+} is summarized in Table 2. It is noted that the fitting ratios of Fe^{3+}/Fe^{2+} and Co^{3+}/Co^{2+} over the supported catalysts (Fe^{3+}/ Fe^{2+} = 0.84– 1.00; Co^{3+}/Co^{2+} = 0.68–1.04) are higher than that of the 3DOM LSFCO sample (Fe^{3+}/Fe^{2+} = 0.76; Co^{3+}/Co^{2+} = 0.68), indicating that loading of Co$_3$O$_4$ promotes the formation of high va-lence Fe^{3+} and Co^{3+} cations. Among all prepared catalysts, the 10Co$_3$O$_4$/3DOM LSFCO sample possesses the highest surface ratio of Fe^{3+}/Fe^{2+} (1.00) and Co^{3+}/Co^{2+} (1.04), which contribute to the formation of more active oxygen vacancies, accelerating the oxygen

atom transfer from gas phase to catalyst surface.

O 1s XPS spectra (Fig. 5D) reveals that all 3DOM samples exhibits three oxygen bonding features with binding energy at 529.3, 531.6 and 533.2 eV, attributing to the lattice oxygen species (O$_{latt}$), surface ad-sorbed oxygen species (O$_{ads}$, e.g., O^{2-}, O$_2{}^{2-}$, and O$^-$) and surface adsorbed molecular water or surface carbonate species, respectively [27,31,42]. The surface adsorbed oxygen species regarded the electro-philic species can facilitate the deep oxidation of organics [32]. As shown in Table 3, the O$_{ads}$/O$_{latt}$ molar ratios of all supported catalysts (1.27–1.32) are obviously higher than that of the 3DOM LSFCO (1.15),
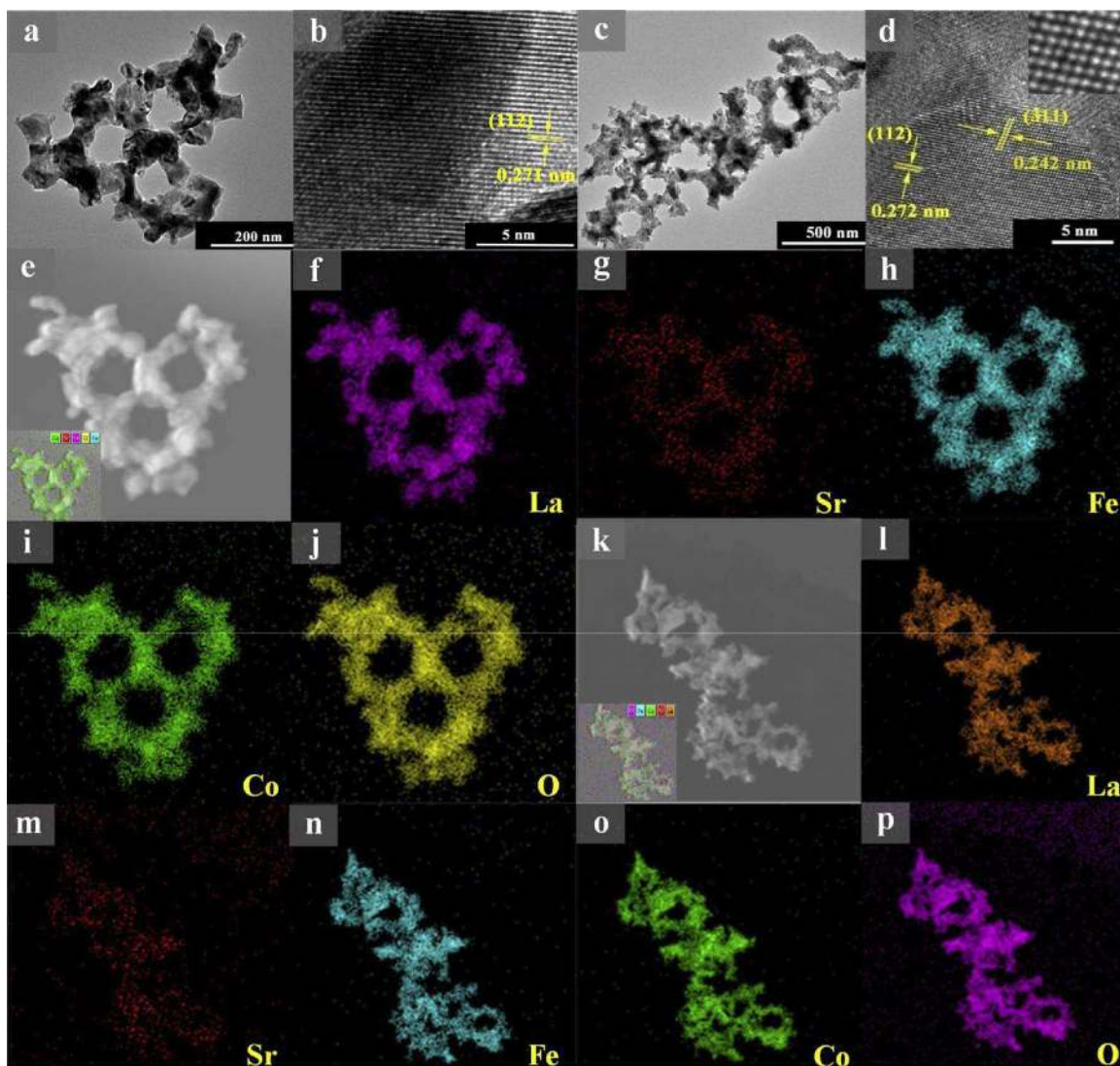
Fig. 3. Typical HR-TEM images of 3DOM LSFCO (a and b) and 10Co₃O₄/3DOM LSFCO (c and d); EDS elemental mappings of 3DOM LSFCO (f–j) and 10Co₃O₄/3DOM LSFCO (l–p) respectively obtain from e and k (STEM).

and the $10Co_3O_4/3DOM$ LSFCO owns the highest O_{ads}/O_{latt} molar ratio (1.32), demonstrating that the large quantity of oxygen vacancies (caused by high valence cations) play a vital role in adsorption of gas phase oxygen.

3.3. Reducibility

The reducibility of all prepared catalysts was characterized by H₂-TPR, as shown in Fig. 6A. Since the metals at A-site of perovskite-type oxide usually have stable valence (herein, La^{3+} and Sr^{2+}) and are non-reducible under the H₂-TPR condition [32], the observed peaks can be attributed to the reduction of Fe^{x+} and Co^{x+} species of the $yCo_3O_4/3DOMLSFCO$ samples. According to the previous work, the reduction process for $La_{0.7}Sr_{0.3}FeO_3$ samples could be divided into two main re-gions: the low temperature region (< 500 °C) for the reduction of Fe^{4+} to Fe^{3+} and the high temperature region (> 500 °C) for the reduction of Fe^{3+} to Fe^{2+} because the Fe^{3+} species was proved to be harder to reduce under low temperature [43]. In this work, the reduction of Fe ions in the samples is attributed to the reduction of Fe^{3+} as no Fe^{4+} can be found in all catalysts (Fig. 5B). In addition, it was reported that the cobalt-based catalysts mainly possess two reduction processes in the range of 300– 650 °C, that is, the Co_3O_4 is firstly reduced to CoO ($Co^{3+} \rightarrow Co^{2+}$) in the temperature range of 300–400 °C, and then the

CoO is further reduced to metallic Co ($Co^{2+} \rightarrow Co°$) between 450 and 650 °C [44]. As displayed in Fig. 6A, all 3DOM catalysts (except $16Co_3O_4/3DOM$ LSFCO) have three reduction peaks between 370 and 610 °C. For the 3DOM LSFCO sample, the first tiny reduction peak at 404 °C corresponded to the reduction of Co_3O_4 to CoO with removing of surface adsorbed oxygen, the second peak at 495 °C can be attributed to the reduction of CoO to metallic cobalt as well as the consumption of the bulk lattice oxygen [38], and the third peak at 598 °C may assign to the reduction of Fe^{3+} to $Fe^{2+}/Fe°$ [45]. The position of low-tempera-ture reduction peaks shifts to low temperature side after loading of Co_3O_4, indicating that the strong interaction between Co_3O_4 and 3DOM LSFCO supporter promotes the reducibility of catalysts (Fig. 6A). Ob-viously, the first reduction temperature decreases with increasing Co_3O_4 loading of 0–10 wt.% (3DOM LSFCO (404 °C), $5Co_3O_4/3DOM$ LSFCO (402 °C), $8Co_3O_4/3DOM$ LSFCO (390 °C), $10Co_3O_4/3DOM$ LSFCO (379 °C)) and increases with the Co_3O_4 loading of 12–16 wt.%. $10Co_3O_4/3DOM$ LSFCO sample possesses the lowest reduction tem-perature, illustrating that optimized loading of Co_3O_4 can maximize the mobility of the surface oxygen and further facilitated the transforma-tion of the surface oxygen. Furthermore, the formation of chemisorbed oxygen on the catalyst surface can contribute to the most reducible sample. Higher metal loading (e.g. 12 wt.% or 16 wt.% of Co_3O_4) could lead to partial aggregation and lower dispersion of active metal phase,
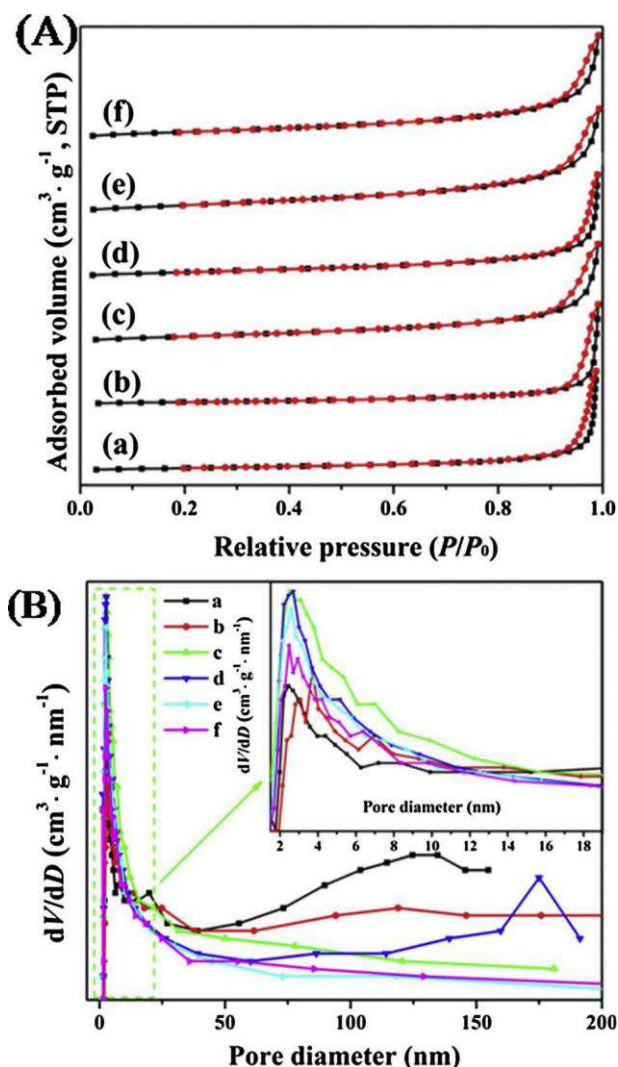
Fig. 4. Nitrogen adsorption−desorption isotherms (A) and Pore size distribution (B) of (a) 3DOM LSFCO, (b) $5Co_3O_4$/3DOM LSFCO, (c) $8Co_3O_4$/3DOM LSFCO, (d) $10Co_3O_4$/3DOM LSFCO, (e) $12Co_3O_4$/3DOM LSFCO, and (f) $16Co_3O_4$/3DOM LSFCO.

which would result in a partial blocking of mesopores, limiting the diffusion and transfer of O_2 and hindering the oxidation of 1,2-DCE.

To further investigated the reducibility of the catalysts, H_2 con-sumptions below 500 °C were determined (Table 3). If Co_3O_4 is assumed the only active component in the materials, H_2 consumption would be 18.67 and 12.45 mmol/g (if the cobalt ions in cobalt oxide with only Co^{3+} and only Co^{2+} were reduced to $Co°$), respectively. The H_2 con-sumptions of the $5Co_3O_4$/3DOM LSFCO (1.46 mmol/g), $8Co_3O_4$/3DOM LSFCO (1.42 mmol/g), and $10Co_3O_4$/3DOM LSFCO (1.87 mmol/g) are higher than the theoretical values (0.933, 1.493, and 1.867 mmol/g) indicating that the 3DOM LSFCO (if the iron ions and cobalt ions in the perovskite were only Fe^{2+} and only Co^{2+} and reduced to $Fe°$ and $Co°$ or the iron ions and cobalt ions in the perovskite were only Fe^{4+} and only Co^{3+} and reduced to $Fe°$ and $Co°$, the theoretical value of H_2 con-sumption of 3DOM LSFCO is from 2.57 to 4.49 mmol/g, respectively) is also participated in the reduced process. The H_2 consumptions of the $12Co_3O_4$/3DOM LSFCO (1.85 mmol/g) and $16Co_3O_4$/3DOM LSFCO (1.50 mmol/g) are lower than the theoretical value (2.240 and 2.987 mmol/g) suggesting the active component didn't be totally re-duced in the process. According to the H_2 consumptions of the mate-rials, the reducibility of these catalysts is in the sequence of $10Co_3O_4$/ 3DOM LSFCO > $12Co_3O_4$/3DOM LSFCO > $16Co_3O_4$/3DOM LSFCO > $5Co_3O_4$/3DOM LSFCO > $8Co_3O_4$/3DOM LSFCO > 3DOM

LSFCO.

The initial (where less than 25% oxygen for the first reduction peak in the sample was removed) H_2 consumption rate was calculated to better evaluate the low-temperature reducibility of the samples, as depicted in Fig. 6B [26]. It is clearly seen that the initial H_2 con-sumption rates of the samples decreased in the order of $10Co_3O_4$/3DOM LSFCO > $16Co_3O_4$/3DOM LSFCO > $12Co_3O_4$/3DOM LSFCO > $8Co_3O_4$/3DOM LSFCO > $5Co_3O_4$/3DOM LSFCO > 3DOM LSFCO. Such a trend in low-temperature reducibility is in good consistence with those in O_{ads} (Table 3) concentration (except for $8Co_3O_4$/3DOM LSFCO).

3.4. Oxygen species

O_2-TPD measurements were performed to investigate the oxygen species of the perovskite samples. It is reported that the adsorbed oxygen generally changes in the following procedures: O_2 (ads) $\rightarrow O_2^-$ (ads) $\rightarrow O^-$ (ads) $\rightarrow O^{2-}$ (lattice) [46]. The physically adsorbed oxygen (O_2 (ads)) are ascribed to oxygen species bounded to the surface of perovskite weakly and the oxygen species (O_2^- and O^-) regarded as the chemical adsorbed oxygen reflects not only the number of oxygen vacancies generated in the catalyst but also the difficulty of re-generating oxygen vacancies, which can be desorbed more easily below 600 °C [47–49]. However, the desorption of lattice oxygen usually oc-curs at higher temperatures (> 700 °C) [49]. As shown in Fig. S3, three peaks of oxygen species are observed at around 52–200, 300–521, and 695–825 °C assigned to physically adsorbed oxygen (O_{ads-p}), chemical adsorbed oxygen (O_{ads-c}), and lattice oxygen (O_{latt}), respectively. The desorbed chemical adsorbed oxygen over the samples could ascribed to the oxygen originating from the oxygen vacancies on the surface or in the subsurface, which contribute to the activity level for 1,2-DCE oxi-dation [41,50]. Therefore, the chemical adsorbed oxygen play a vital role in the reaction process. The areas of the oxygen species were fur-ther estimated by integral. The $10Co_3O_4$/3DOM LSFCO own the max-imum area (19.56) similar to $12Co_3O_4$/3DOM LSFCO (19.26), which is higher than 3DOM LSFCO (10.02), $5Co_3O_4$/3DOM LSFCO (13.01), $8Co_3O_4$/3DOM LSFCO (13.57) and $16Co_3O_4$/3DOM LSFCO (17.50). The results are almost consistent with the catalytic activity of the 1,2-DCE, which suggests that the oxygen vacancies over the samples is of the most importance in the reaction process.

3.5. Catalytic activity and stability

The catalytic activities in the oxidation of 1,2-DCE over prepared 3DOM catalysts are shown in Fig. 7A, and the temperatures for 10%, 50%, and 90% conversions (T_{10}, T_{50}, and T_{90}) of 1,2-DCE are sum-marized in Table 1. All Co_3O_4-loaded catalysts have better catalytic activity than the 3DOM LSFCO, which can be explained by the fact that the introduction of Co_3O_4 promotes the reduction of Co^{3+} and Co^{2+} species ascribable to the increasing of surface adsorbed oxygen species and the strong interaction between Co_3O_4 and 3DOM LSFCO (Figs. 5 and 6). Among the supported samples, $10Co_3O_4$/3DOM LSFCO and $12Co_3O_4$/3DOM LSFCO exhibit the best catalytic activity, while the $10Co_3O_4$/3DOMLSFCO sample performs higher activity when reaction temperatures exceed 450 °C, which is associated with the maximum concentration of surface active oxygen (XPS and H_2-TPR). The catalytic activity of $5Co_3O_4$/3DOM LSFCO and $8Co_3O_4$/3DOM LSFCO is lower than $10Co_3O_4$/3DOM LSFCO on account of the limited content of the active components. The higher content of the active components could lead to larger particles and lower dispersed species of metal oxides, which would limit the catalytic activity of $12Co_3O_4$/3DOM LSFCO and $16Co_3O_4$/3DOM LSFCO [51]. The catalytic activity of non-3DOM LSFCO (N3DOM LSFCO) using the sol-gel method was also investigated and the conversion plot was present in Fig. S4. As shown, it can be clearly observed that 3DOM LSFCO owns better conversion of 1,2-DCE than N3DOM LSFCO, indicating that the three-dimensional ordered
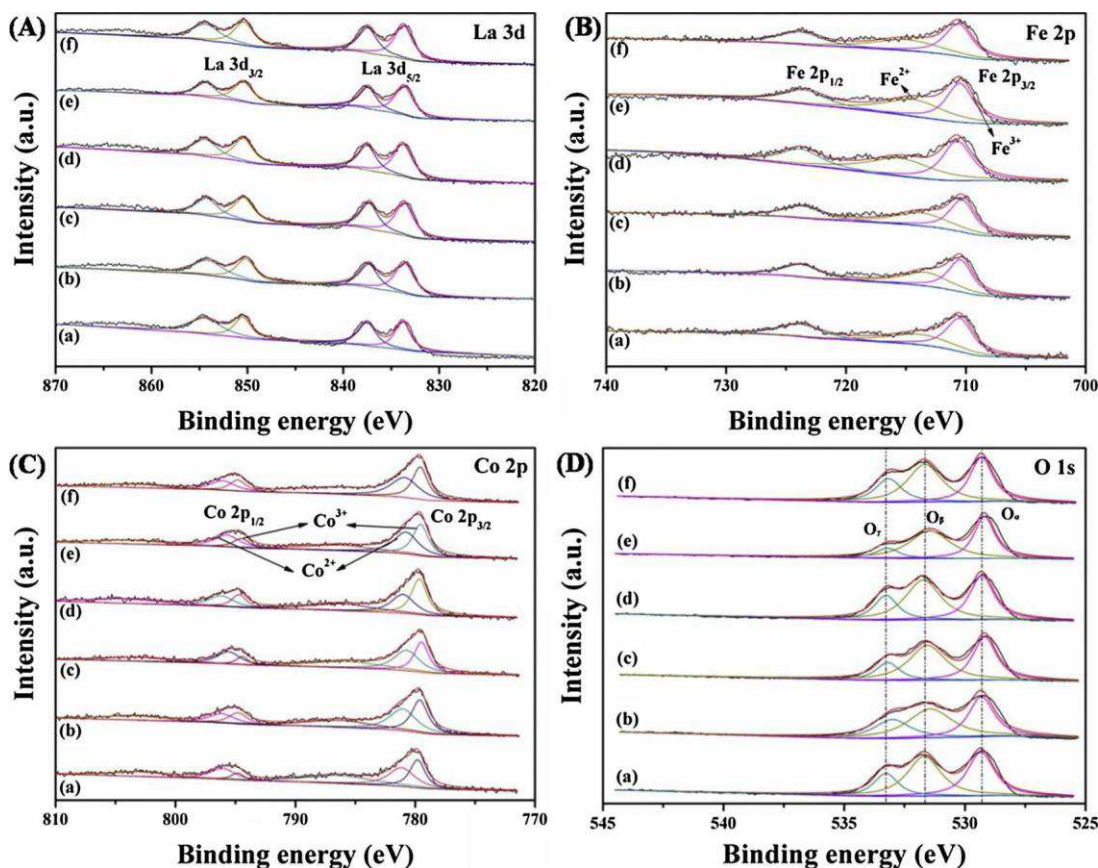
Fig. 5. (A) La 3d, (B) Fe 2p, (C) Co 2p and (D) O 1s XPS spectra of (a) 3DOM LSFCO, (b) 5Co$_3$O$_4$/3DOM LSFCO, (c) 8Co$_3$O$_4$/3DOM LSFCO, (d) 10Co$_3$O$_4$/3DOM LSFCO, (e) 12Co$_3$O$_4$/ 3DOM LSFCO, and (f) 16Co$_3$O$_4$/3DOM LSFCO.

meso-macroporous structure of the material is beneficial to the de-composition of 1,2-DCE.

The oxidation of 1,2-DCE over the 3DOM LSFCO samples follows a first-order reaction mechanism with respect to 1,2-DCE concentration (c): r = kc = (−A$_{exp}$(−E$_a$/RT))c, where r, k, A, E$_a$ are the reaction rate (mol s^{-1}), the rate constant (s^{-1}), the pre-exponential factor and the apparent activation energy (kJ mol^{-1}), respectively. Fig. 7B shows the reaction rates plot at the reaction temperature of 300 °C. It is clearly observed that the reaction rates of the Co$_3$O$_4$-loaded 3DOM LSFCO catalysts are higher than that of 3DOM LSFCO, and 10Co$_3$O$_4$/3DOM LSFCO possesses the highest reaction rate, suggesting that the in-troduction of Co$_3$O$_4$ is favorable for the reaction. The values of apparent activation energy (E$_a$) for the catalysts can be also generated by the temperature dependence of the reaction rate, taking 1,2-DCE con-centration having no obvious change within 20% conversion. As listed in Table 1, E$_a$ values of the samples are in the range of 22.6–74.7 kJ mol^{-1} and the E$_a$ increases in the sequence of 10Co$_3$O$_4$/ 3DOM LSFCO (22.6 kJ mol^{-1}) < 12Co$_3$O$_4$/3DOM LSFCO < 5Co$_3$O$_4$/

3DOM LSFCO < 16Co$_3$O$_4$/3DOM LSFCO < 8Co$_3$O$_4$/3DOM LSFCO < 3DOM LSFCO. It is obviously observed the E$_a$ value of 3DOM LSFCO is much higher than that of the Co$_3$O$_4$-based samples, indicating that the 1,2-DCE is more easily oxidized by the supported Co catalysts.

The concentration variation of CO and CO$_2$ in the oxidation of 1,2-DCE was further investigated, as displayed in Fig. 8. CO concentration increases obviously along with the increasing of temperature, and then decreases quickly when the temperature is higher than 500 °C due to the further oxidation reaction of CO to CO$_2$ in the presence of active oxygen species. The CO concentration over the 3DOM LSFCO sample is much higher than the other catalysts at different temperature points with highest CO concentration of 145 ppm at 500 °C. CO concentration over the yCo$_3$O$_4$/3DOM LSFCO catalysts generally follows the sequence

of 3DOM LSFCO > 5Co$_3$O$_4$/3DOM LSFCO > 10Co$_3$O$_4$/3DOM LSFCO > 8Co$_3$O$_4$/3DOM LSFCO > 12Co$_3$O$_4$/3DOM LSFCO > 16Co$_3$O$_4$/3DOM LSFCO, and lower concentration of CO over the Co$_3$O$_4$-loaded catalysts is attributed to the strong active oxygen capa-city of Co$_3$O$_4$ phase. The formation of CO$_2$ increases slowly with the temperature increasing from 200 to 400 °C, and just tiny amounts of CO$_2$ can be detected when the temperature is lower than 300 °C as 1,2-DCE is mainly destructed to vinyl chloride, 1,1,2- trichloroethane, and trichloroethylene. It is important to notice that the concentration of CO$_2$ increases sharply when the temperature is higher than 400 °C, especially for the 10Co$_3$O$_4$/3DOM LSFCO and 12Co$_3$O$_4$/3DOM LSFCO catalysts. Meanwhile, it can be clearly observed that the amount of the CO$_2$ products over each samples had a big difference, which can be also discovered in Table 1. As shown in Table 1, the 10Co$_3$O$_4$/3DOM LSFCO is suggested the highest selectivity of CO$_2$ (77.1%) and 3DOM LSFCO shows the lowest CO$_2$ selectivity (25.4%) at 500 °C in according with the results shown in Fig. 8, which is considered the little surface ad-sorbed oxygen and active sites over the 3DOM LSFCO.

The concentration of CO$_2$ over 3DOM LSFCO and 10Co$_3$O$_4$/3DOM LSFCO samples was also on-line analyzed by an MS system, as shown in Fig. 9. The 1,2-DCE oxidation was conducted in the temperature range of 160–580 °C, and the reaction was steadied for 40 min at each tem-perature. It can be observed that 1,2-DCE is distinctly oxidized in the reaction process and just a little amount of CO$_2$ is detected before 350 °C, while the CO$_2$ concentration enhances obviously when the re-action temperature exceeds 350 °C, in good agreement with the GC results (Fig. 8). Moreover, it is noticeable that the CO$_2$ yield over the 10Co$_3$O$_4$/3DOM LSFCO catalyst is better than that over the 3DOM LSFCO sample at elevated temperature range (400–580 °C). As is known, the introduction of Co$_3$O$_4$ to 3DOM LSFCO enhances the ad-sorption of gas species (1,2-DCE and oxygen species) and oxygen
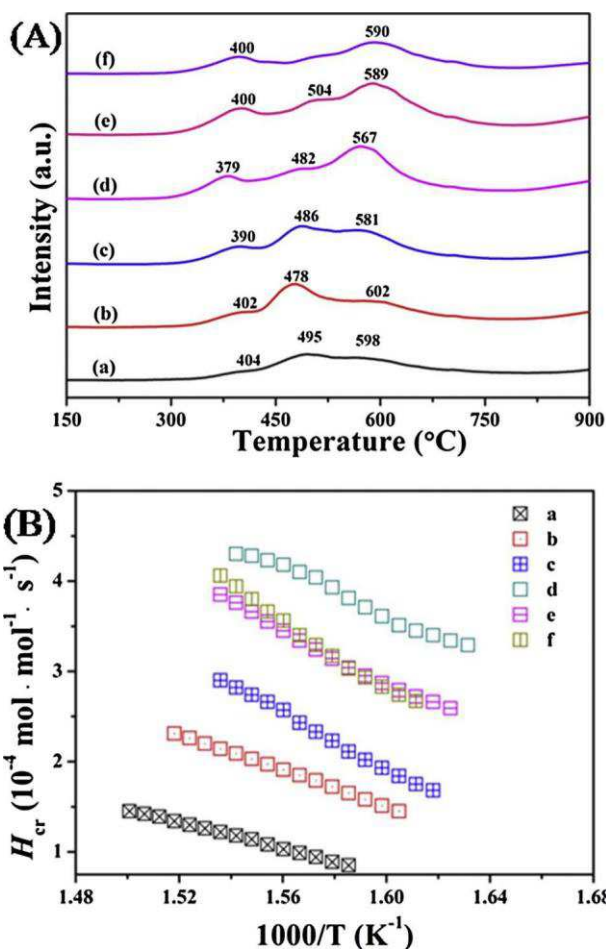
Fig. 6. (A) H2-TPR profiles and (B) initial H2 consumption rate (Hcr) as a function of inverse temperature of (a) 3DOM LSFCO, (b) 5Co3O4/3DOM LSFCO, (c) 8Co3O4/3DOM LSFCO, (d) 10Co3O4/3DOM LSFCO, (e) 12Co3O4/3DOM LSFCO, and (f) 16Co3O4/3DOM LSFCO.

Fig. 7. (A) Light-off curves of 1,2-DCE oxidation and (B) reaction rate (Rr) at 300 °C over (a) 3DOM LSFCO, (b) 5Co3O4/3DOM LSFCO, (c) 8Co3O4/3DOM LSFCO, (d) 10Co3O4/3DOM LSFCO, (e) 12Co3O4/3DOM LSFCO, and (f) 16Co3O4/3DOM LSFCO.

mobility, which accelerates the oxidation process of organics and en-hances the yield of CO_2. HCl and Cl_2 regarded as the primary total oxidation produces of chlorinated organic compounds were also in-vestigated. As shown in Fig. 9, the intensity of HCl over the 3DOM LSFCO is continually increased but its concentration is lower than 10Co3O4/3DOM LSFCO. Notably, although the HCl concentration over 10Co3O4/3DOM LSFCO is also increased, it reveals a first drop at around 400 °C, which can be interpreted as the existence of the Deacon reaction (2HCln + O_2 ↔Cl_2 + H_2O) resulting in the formation of Cl_2. Corresponding to the analytical result of HCl, the Cl_2 concentration over the 10Co3O4/3DOM LSFCO can't be almost detected before 400 °C but have a tiny increasing tend after 400 °C, proving the existence of the Deacon reaction. By contrast, the Cl_2 on 3DOM LSFCO can be detected sustainably in the oxidation process. However, Cl_2 is a total oxidation produce out of favor because of its high corrosivity and toxicity. Therefore, 10Co3O4/3DOM LSFCO is more suitable for the oxidation of chlorinated products.

The catalytic stability of the best performed 10Co3O4/3DOM LSFCO catalyst in the oxidation of 1,2-DCE was studied, as displayed in Fig. 10A. It can be observed that the conversion of 1,2-DCE over 10Co3O4/3DOM LSFCO almost maintains at about 85% within the whole testing period, showing an excellent 1,2-DCE oxidation stability. The strong interaction between Co3O4 and 3DOM LSFCO enhances the durability and chlorine resistance of the composite catalyst. To check the structure stability of the catalyst, the XRD analysis of the spent 10Co3O4/3DOM LSFCO after stability test was further carried out. As shown in Fig. 10B, good orthorhombic crystal phase of perovskite
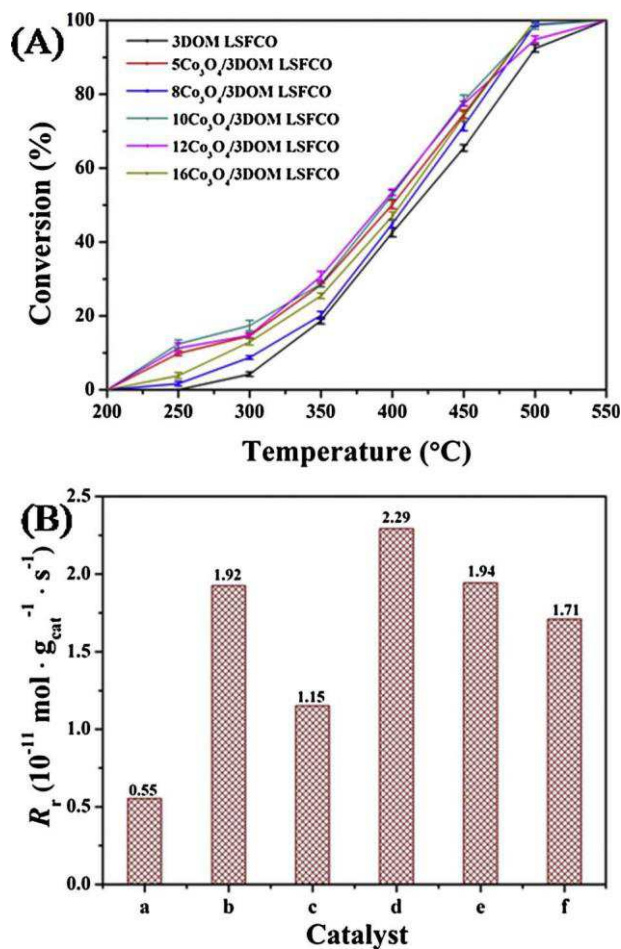
(JCPDS PDF No. 01-089-1267) is well maintained, indicating the su-perior structure stability and resistance to chlorine poisoning of the 10Co3O4/3DOM LSFCO catalyst. Three new distinctly diffraction peaks are observed over the spent 10Co3O4/3DOM LSFCO sample compared with the fresh catalyst, which ascribes to the adsorption of chlorine species on the surface of cobalt sites [52]. It is known that the de-struction of chlorinated compounds would result in the surface cobalt oxides sites adsorbing chlorine but the detected chlorine species don't reduce the conversion of 1,2-DCE, indicating the catalyst possesses good resistance to chlorine poisoning.

3.6. Correlation of physicochemical property and catalytic activity

The oxygen species in the catalysts are considered playing a critical role in the deep oxidation of 1,2-DCE. The relationship between the O_{ads}/O_{latt} ratio and the CO_2 selectivity at 500 °C is investigated, as shown in Fig. 11. According to the calculated linearity (coefficient of determination, R^2 = 0.9251), O_{ads}/O_{latt} ratio are correlated to CO_2 se-lectivity, and the O_{ads}/O_{latt} ratio of Co3O4-loaded catalysts are higher than 3DOM LSFCO, which perform higher CO_2 selectivity. Especially, the 10Co3O4/3DOM LSFCO catalyst with the highest O_{ads}/O_{latt} ratio exhibits a higher CO_2 selectivity (contrary to 3DOM LSFCO), suggesting that the oxygen species is responsible for the catalytic activity and a high O_{ads}/O_{latt} ratio leads to a higher oxidative activity in accordance with the catalytic activity, XPS and H_2-TPR results.

The Cl atom of 1,2-DCE adsorbed on the surface oxygen species or hydroxyl groups from the surface of catalysts perform a nucleophilic attacked on the carbon atom of 1,2-DCE and then dehydrochlorination

Table 1
Textural property and catalytic performance of synthesized catalysts.

Sample	S_{BET}^a (m²/g)	D_v^b (cm³/g)	D_p^c (nm)	$T_{10\%}^d$ (°C)	$T_{50\%}^d$ (°C)	$T_{90\%}^d$ (°C)	Selectivity (%)			E_a^g (KJ/mol)
							CO^e	CO_2^e	HCl^f	
3DOM LSFCO	13.3	0.13	18.9	321	416	496	15.4	25.4	0.24	74.7
5Co3O4/3DOM LSFCO	11.9	0.15	25.3	254	399	481	12.2	58.4	0.25	28.4
8Co3O4/3DOM LSFCO	17.7	0.08	8.6	306	410	484	8.9	63.7	0.31	68.4
10Co3O4/3DOM LSFCO	16.3	0.09	10.5	241	390	478	9.2	77.1	0.34	22.6
12Co3O4/3DOM LSFCO	13.9	0.05	6.9	245	393	486	8.6	67.3	0.30	26.7
16Co3O4/3DOM LSFCO	12.6	0.05	8.0	284	406	481	6.0	58.1	0.28	51.7

Note: [a]Specific surface area obtained at P/P0 = 0.05–0.30; [b]Total pore volume estimated at P/P0 = 0.99; [c]BJH pore diameter calculated from the desorption branch; [d]Temperatures at which 10%, 50% and 90% conversion of 1,2-DCE; [e]CO and CO2 selectivity over various catalysts in the oxidation of 1,2-DCE at 500 °C; [f]HCl selectivity over various catalysts in the oxidation of 1,2-DCE at 400 °C; [g]Apparent activation energy obtained from Arrhenius plot.

Table 2
Co 2p XPS results of prepared catalysts.

Sample	Co 2p1/2 (eV)		Co 2p3/2 (eV)		Co^{3+}/Co^{2+}
	Co^{2+}	Co^{3+}	Co^{2+}	Co^{3+}	
3DOM LSFCO	796.1 (2167)	794.8 (697)	781.1 (3939)	779.8 (3455)	0.68
5Co3O4/3DOM LSFCO	796.1 (2679)	794.8 (2272)	781.0 (6580)	779.6 (6067)	0.90
8Co3O4/3DOM LSFCO	795.6 (2613)	794.4 (952)	780.7 (5174)	779.5 (4368)	0.68
10Co3O4/3DOM LSFCO	796.2 (2146)	794.7 (1480)	781.0 (3579)	779.7 (4483)	1.04
12Co3O4/3DOM LSFCO	795.7 (3471)	794.5 (1758)	780.8 (6196)	779.5 (5788)	0.78
16Co3O4/3DOM LSFCO	796.1 (2629)	794.8 (1982)	780.9 (6217)	779.6 (5588)	0.86

Note: The data in the parentheses are the peak area at corresponding banding energies.

Fig. 8. CO and CO2 distribution over the synthesized catalysts: (a) 3DOM LSFCO, (b) 5Co3O4/3DOM LSFCO, (c) 8Co3O4/3DOM LSFCO, (d) 10Co3O4/3DOM LSFCO, (e) 12Co3O4/3DOM LSFCO, and (f) 16Co3O4/3DOM LSFCO.

occurs, which suggest the adsorption of 1,2-DCE plays an important role in the catalytic reaction process [53]. To investigate the adsorption and activation behaviors over 3DOM LSFCO and 10Co3O4/3DOM LSFCO catalysts, 1,2-DCE low-temperature adsorption were in-vestigated by in situ DRIFTS at different time intervals, as shown in Fig. 12. As shown in Fig. 12A, the surface species concentration over the 3DOM LSFCO is almost steady from 0 to 30 min and then gradually increases until to 90 min, indicating that 1,2-DCE is nearly adsorbed firstly and then began to band with the chemisorbed oxygen species on the surface of the sample [54]. Several bands at 3737, 3626, 3587 and 3566 cm⁻¹ are assigned to the formation of H bonded hydroxyls [55], and the band at 1548 cm⁻¹ is corresponded to $\nu(COO)_{ads}$ of surface acetate species [56]. The band located at 1309 cm⁻¹ can be assigned to δ(CH2Cl), δ(HCCl), δ(CCH) and ν(CC) + (CCH) corresponding to the adsorbed 1,2-DCE. The band at 1198 cm⁻¹ can be corresponded to phenolate (ν(CH)/ν(CO)), and the bands centered at 1127 and 1046 cm⁻¹ can be respectively assigned to the bending vibrations of C−H in-plant and ρ(CH2) [14,57]. The concentration of surface

adsorbed species over the 10Co3O4/3DOM LSFCO sample is con-tinuously increased from beginning to 90 min (Fig. 12B), indicating that the superior adsorption capacity and mobility of surface oxygen species contribute to accelerate the oxidation of 1,2-DCE, resulting in the in-creasing of chlorinated species. The bands at 3900, 3737, 3626, and 3669 cm⁻¹ are assigned to the formation of H bonded hydroxyls, and the bands at 3626, 3566, 3543, 3523, and 3505 cm⁻¹ can also be as-cribed to different types of surface hydroxyl [55,58]. The bands at 1548 and 1373 cm⁻¹ are assigned to $\nu(COO)_{ads}$ of surface acetate species, and the bands at 1476, 1290, 1269, and 1124 cm⁻¹ are ascribed to −CH− vibration in 1,2-DCE [58]. The bands located at 1426, 1361, 1309, 1046, 1019, and 941 cm⁻¹ can be assigned to the deformation of −CH2− and −CH− groups in 1,2-DCE [14,54,55]. The band at 1338 cm⁻¹ can be assigned to partially oxidized formates, acetates, and maleates [41]. The band at 1257 cm⁻¹ is assigned to CH−Cl vibration,

Table 3
O1s XPS and H2-TPR results of prepared catalysts.

Sample	O 1s (eV)			$O_s/O_α$	H_c^d (mmol/g)
	$O_α^a$	$O_β^b$	$O_γ^c$		
3DOM LSFCO	529.3 (14070)	531.7 (16213)	533.3 (6675)	1.15	0.85
5Co3O4/3DOM LSFCO	529.3 (15880)	531.4 (20401)	533.0 (10703)	1.28	1.46
8Co3O4/3DOM LSFCO	529.2 (13520)	531.5 (17183)	533.2 (5652)	1.27	1.42
10Co3O4/3DOM LSFCO	529.3 (12763)	531.7 (16883)	533.3 (3968)	1.32	1.87
12Co3O4/3DOM LSFCO	529.2 (14700)	531.5 (19178)	533.2 (3968)	1.30	1.85
16Co3O4/3DOM LSFCO	529.3 (14757)	531.7 (18978)	533.2 (9043)	1.29	1.50

Note: The lattice oxygen[a], surface adsorbed oxygen[b], and surface adsorbed molecular water or surface carbonate species[c] (data in the parentheses are the peak area at corresponding banding energies); [d]H2 consumption amount below 500 °C over various catalysts.
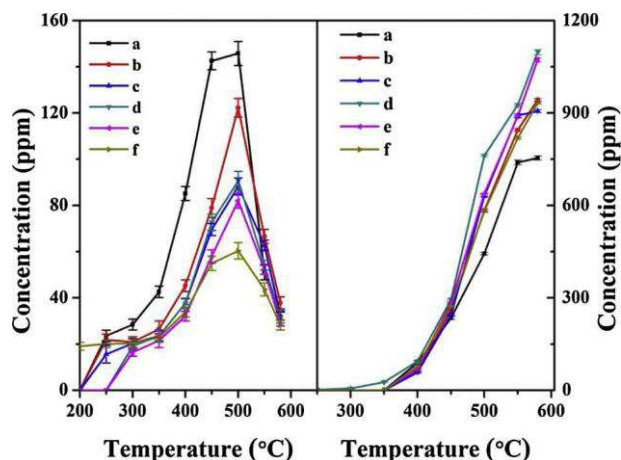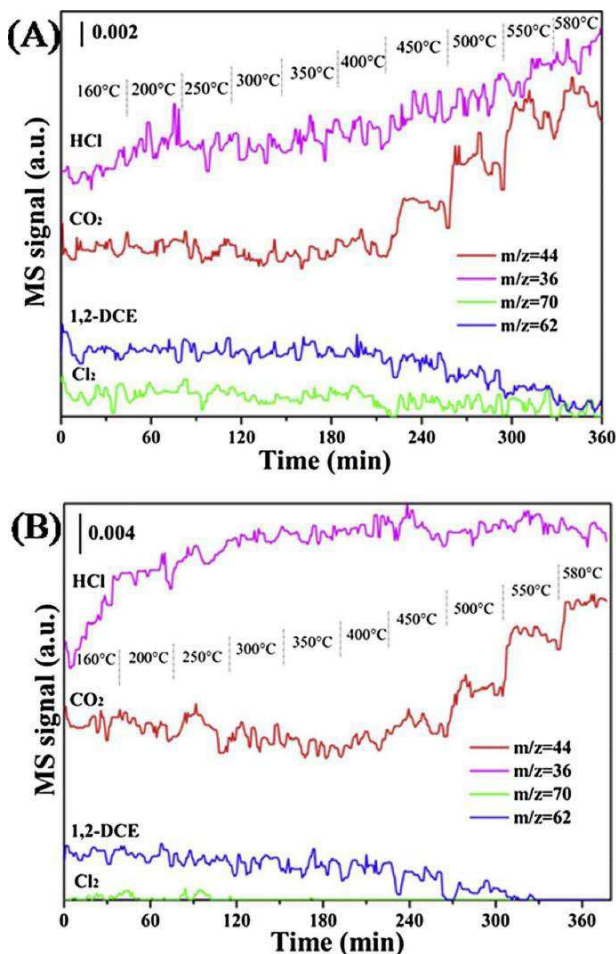
Fig. 9. On-line MS results of typical oxidation products in temperature range of 160–580 °C over (A) 3DOM LSFCO and (B) 10Co₃O₄/3DOM LSFCO.

and the existence of phenolate (v(CH)/v(CO)) can be observed with the main band located at 1189 cm^{-1} and a shoulder band at 1204 cm^{-1} [56]. The CeCl$_2$ band in 1,2-DCE is found at 916 cm^{-1}, and the band at 892 cm^{-1} is assigned to the stretching of $CeCl$ band [54]. Chintawar et al. found a strong relationship between the adsorption capacity and the reactivity of the reactant molecule on the catalyst: the strength of adsorption on the catalyst increases and thus augments the catalytic activity [59]. As shown in Fig. 12, the adsorption concentrations of 1,2-DCE on the surface of 3DOM LSFCO are obviously lower than that over the 10Co₃O₄/3DOM LSFCO, which suggests that introducing Co₃O₄ to 3DOM LSFCO increases the adsorption capacity of the sample and then facilitate the oxidation reaction of 1,2-DCE.

3.7. Intermediate species and oxidation mechanism

During catalytic oxidation of CVOCs, it is usually impossible to avoid the formation of chlorinated by-products, especially over sup-ported metal catalysts. In this work, several primary chlorinated by-products such as vinyl chloride (VC), 1,1,2-trichloroethane, tri-chloroethylene, tetrachloroethylene, trichloromethane and tetra-chloromethane were detected during 1,2-DCE oxidation by GC at dif-ferent time (Fig. S5, Fig. S6 and Fig. 13). The relationship between the chlorinated by-products distribution and reaction temperature are presented in Fig. 13 and the chlorination pathways exhibit in Scheme Scheme 2. In general, the concentration of all intermediate products increases with the increasing of reaction temperature firstly and then decreases continuously when further elevate the reaction temperature. Almost the same kinds of by-products can be observed over all the
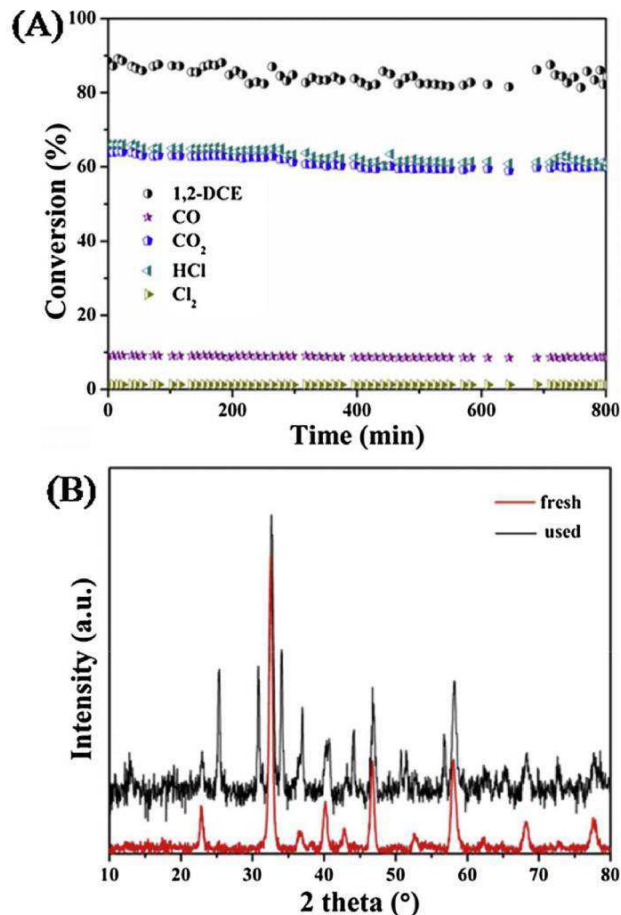

Fig. 10. (A) Stability of 10Co₃O₄/3DOM LSFCO for 1,2-DCE oxidation at 480 °C; (B) XRD patterns of the fresh and used 10Co₃O₄/3DOM LSFCO.

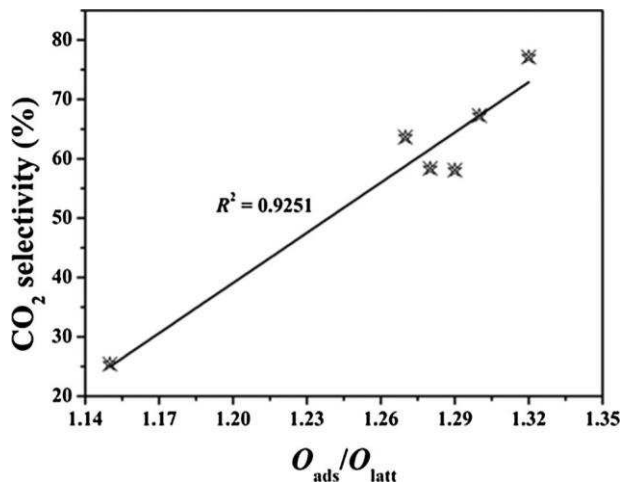Fig. 11. Relationship between the O$_{ads}$/O$_{latt}$ ratio and the CO$_2$ selectivity at 500 °C for the prepared catalysts.

catalysts, however, the concentration of the intermediate products and the tendencies of different products are also varied significantly over catalysts. 10Co₃O₄/3DOM LSFCO possesses the lowest yield of the chlorinated by-products (except tetrachloromethane) and the 3DOM LSFCO catalyst without Co₃O₄ has the highest concentration of by-pro-ducts, indicating that the yield of the chlorinated by-products is in-hibited by Co to some extent and the adsorbed oxygen species in the studied catalysts maybe a key point for the total oxidation of 1,2-DCE. Vinyl chloride is an important intermediate product in the oxidation of
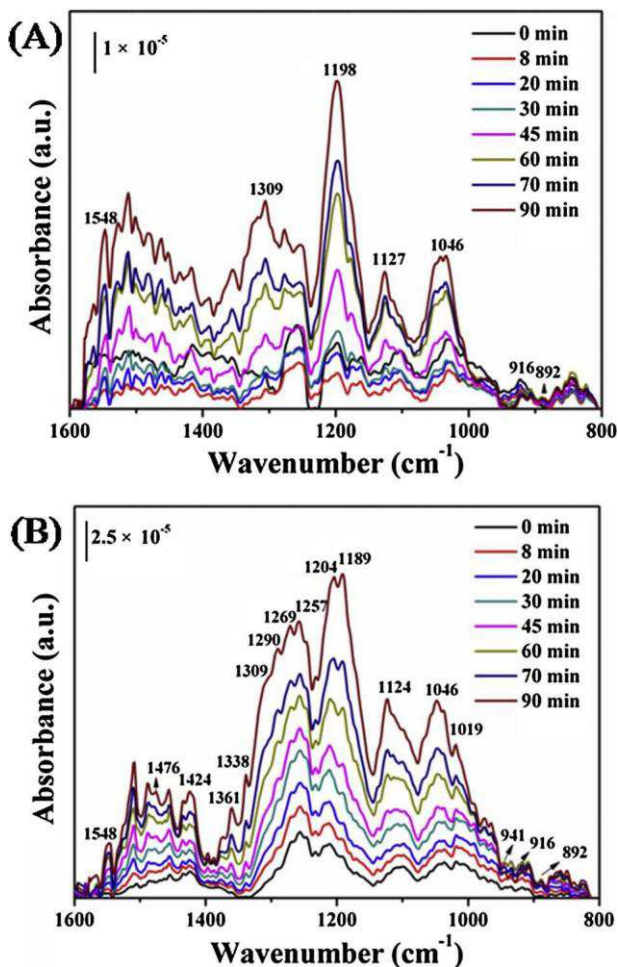
Fig. 12. In situ FT-IR spectra collected at 100 °C for 1,2-DCE adsorption over (A) 3DOM LSFCO and (B) 10Co₃O₄/3DOM LSFCO.
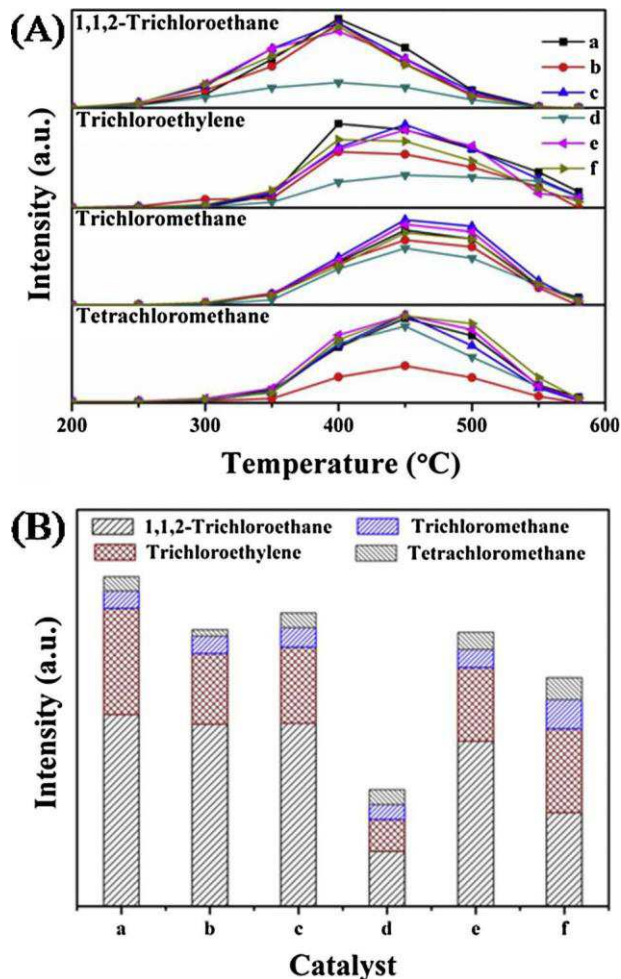

Fig. 13. (A) The main reaction by-products distribution at different temperatures and (B) the main by-products plot at 400 °C over (a) 3DOM LSFCO, (b) 5Co₃O₄/3DOM LSFCO, (c) 8Co₃O₄/3DOM LSFCO, (d) 10Co₃O₄/3DOM LSFCO, (e) 12Co₃O₄/3DOM LSFCO, and (f) 16Co₃O₄/3DOM LSFCO.

1,2-DCE [50,60,61], and the distribution of VC was detected by the on-line mass spectrometer, as shown in Fig. S6. The existence of VC can be clearly observed from the beginning temperature of 160 °C. The in-tensity of VC over 3DOM LSFCO is weaker than that of over 10Co₃O₄/ 3DOM LSFCO, and the decomposition rate of the 3DOM LSFCO catalyst is obviously lower than that of 10Co₃O₄/3DOM LSFCO, indicating that the better oxidation activity of the 10Co₃O₄/3DOM LSFCO promoted the oxidation of 1,2-DCE and limited the generation of the intermediate products. The trend of the VC plot suggests 10Co₃O₄/3DOM LSFCO prefer generating the complete oxidation products (CO_2, CO, HCl and Cl_2).

As depicted in Fig. 13A, 1,1,2-trichloroethane is first detected at 250 °C, which is attributed to the nucleophilic addition reaction of vinyl chloride. The elimination of HCl from VC is promoted by the catalysts. It can be noted that the relative concentration of 1,1,2-trichloroethane reaches the maximum value at 400 °C, and further dehydrochlorination and substitution reaction of 1,1,2-trichloroethane with chlorine pro-motes the formation of trichloroethylene through a concerted elim-ination mechanism (Scheme Scheme 2). The trichloroethylene is mainly generated within the temperature range from 400 to 450 °C. Ad-ditionally, a small amount of tetrachloroethylene is also observed via further dehydrochlorination and chlorination of trichloroethylene at relative high temperature (350 °C). A sequential dehydrochlorination and chlorination are the main reaction processes for the formation of poly-chlorinated by-products. For another reactive pathway, CeC bond cleavage can facilitate the formation of CH_3Cl. Furthermore, the for-mation of trichloromethane and tetrachloromethane can be attributed to the chlorination of CH_3Cl, as the two chlorinated by-products form at

almost the same temperature and exhibit the similar trend of con-centration vs reaction temperature. Obviously, these two undesired intermediate products are totally oxidized at the end of the disin-tegration process. Fig. 13B shows the distribution of by-products of each sample at 400 °C. Mostly, chlorinated by-products formed during the reaction process at this temperature, with the amount of produced dependent on the activity of the catalysts for the oxidation of 1,2-DCE. Obviously, the 10Co₃O₄/3DOM LSFCO possesses the lowest con-centration of the chlorinated intermediate products. And the 3DOM LSFCO is demonstrated a maximum concentration of the 1,1,2-tri-chloroethane as well as the trichloroethylene, which is attribute to the scarce surface oxygen species comparing to the supported Co₃O₄ cata-lysts. Small amount concentration of trichloromethane and tetra-chloromethane are considerably different from 1,1,2-trichloroethane and the trichloroethylene, which suggest that the reactive pathway of CeC bond cleavage is more difficult to conduct than the breaking of CeCl bond pathway in this work.

1,2-DCE oxidation routes based on the successive dehydro-chlorination and chlorination reactions are proposed, as shown in Scheme Scheme 2. The Mars-van Krevelen mechanism (MVK me-chanism) is considered to fit with the reaction process, in which Co₃O₄ supplies oxygen to the reaction and then it is reoxidized by gas phase oxygen. That is, the MVK mechanism based on the redox reaction oc-curs between the adsorbed gas molecules (1,2-DCE and oxygen species) and lattice oxygen of catalyst, which associates with the active phase
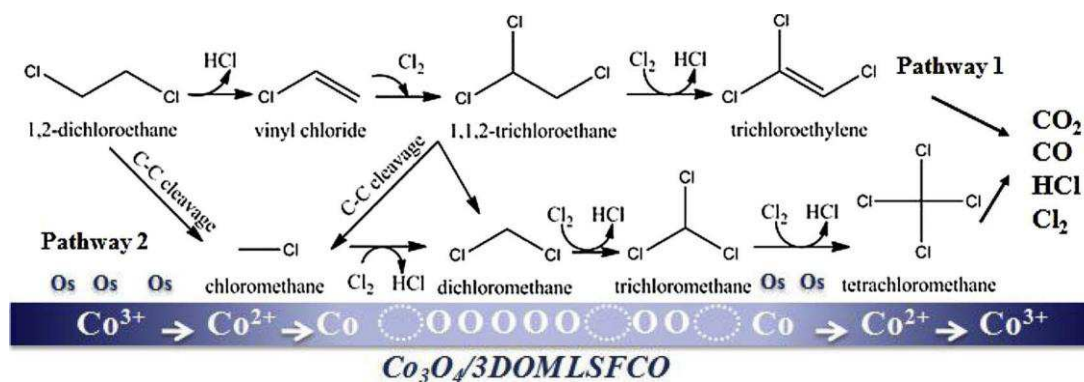
Scheme 2. Proposed mechanism for 1,2-DCE oxidation over Co$_3$O$_4$/3DOM LSFCO catalyst.

and support. 1,2-DCE molecules are adsorbed in the active centers (Co^{3+}) and oxidized by the relevant lattice oxygen species to cleave CeCl bonds or CeC bonds, forming some intermediates (formaldehyde and methoxy groups) that can be oxidized the final products (CO, CO$_2$, HCl, Cl$_2$) or intermediate products (VC, 1,1,2-trichloroethane, tri-chloroethylene, tetrachloroethylene, trichloromethane and tetra-chloromethane, depicted in Fig. 13A) respectively. This leaves behind oxygen vacancies that can not only absorb and activate the adsorbed molecular oxygen, but also can transform them to active chemical oxygen species (O$_2^-$, O^{2-}), which is of great important in the oxidation of 1,2-DCE. The Co^{2+}, Fe^{3+}, or Fe^{2+} center over the 3DOM LSFCO would replenish the dissipative lattice oxygen and receive the gener-ated electron. The adsorbed molecular oxygen in the Co^{2+}, Fe^{3+} or Fe^{2+} center can be transformed to lattice oxygen. Finally, the lattice oxygen would transfer to Co^{3+} active center and the electron transfer to Co^{2+}, Fe^{3+} or Fe^{2+} center forming a redox cycle. Understanding of the first reaction pathway is easier than the second one owing to low bond energy of C-Cl (328 KJ mol^{-1}).

4. Conclusions

Catalytic oxidation of 1,2-DCE over 3DOM LSFCO and Co$_3$O$_4$/ 3DOM LSFCO was investigated. It is suggested that PMMA-templating synthetic method with EG and P123 surfactant could obtain three di-mensional meso-macroporous structural catalyst and the introducing Co$_3$O$_4$ to 3DOM LSFCO can promote the mobility of the surface oxygen to further transform the surface oxygen species to chemisorbed oxygen on the catalyst surface, intensifying the interaction between the Co$_3$O$_4$ and 3DOM LSFCO and enhancing the impact of dehydrochlorination and chlorination in the oxidation reaction of 1,2-DCE. Co$_3$O$_4$-based 3DOM LSFCO materials have been used to demonstrate that the cata-lysts with more surface adsorbed oxygen species resulted in a more prominent adsorption capacity and thus better catalytic activity, along with excellent resistance to chlorine poisoning, all of which play a key role in the total oxidation of 1,2-DCE. 10Co$_3$O$_4$/3DOM LSFCO possesses the lowest E$_a$ (22.6 KJ mol^{-1}), highest reaction rate (2.29 × 10^{-11} mol g^{-1} s^{-1}) at 300 °C, and superior stability. The sur-face oxygen species promote the dehydrochlorination and chlorination reaction and accelerate the generation of the main by-products such as 1,1,2-trichloroethane, trichloroethylene and tetrachloroethylene during oxidation of 1,2-DCE, which finally can be totally oxidized to CO, CO$_2$, HCl and Cl$_2$.

Acknowledgements

References

[1] J. Gonzalez-Prior, J.I. Gutierrez-Ortiz, R. Lopez-Fonseca, G. Busca, E. Finocchio, B. de Rivas, Catal. Sci. Technol. 6 (2016) 5618−5630.
[2] B. de Rivas, C. Sampedro, M. García-Real, R. López-Fonseca, J.I. Gutiérrez-Ortiz, Appl. Catal. B: Environ. 129 (2013) 225−235.
[3] B. Huang, C. Lei, C. Wei, G. Zeng, Environ. Int. 71 (2014) 118−138.
[4] J.R. Gonzalez-Velasco, A. Aranzabal, R. Lopez-Fonseca, R. Ferret, J.A. Gonzalez-Marcos, Appl. Catal. B: Environ. 24 (2000) 33−43.
[5] C. He, Y. Yu, L. Yue, N. Qiao, J. Li, Q. Shen, W. Yu, J. Chen, Z. Hao, Appl. Catal. B: Environ. 147 (2014) 156−166.
[6] C. He, Y. Yu, Q. Shen, J. Chen, N. Qiao, Appl. Surf. Sci. 297 (2014) 59−69.
[7] J. Choi, C.B. Shin, T.-J. Park, D.J. Suh, Appl. Catal. A: Gen. 311 (2006) 105−111.
[8] H. Pan, Y. Jian, C. Chen, C. He, Z. Hao, Z. Shen, H. Liu, Environ. Sci. Technol. 51 (2017) 6288−6297.
[9] S. Pitkäaho, T. Nevanperä, L. Matejova, S. Ojala, R.L. Keiski, Appl. Catal. B: Environ. 138−139 (2013) 33−42.
[10] S. Pitkäaho, L. Matejova, K. Jiratova, S. Ojala, R.L. Keiski, Appl. Catal. B: Environ. 126 (126) (2012) 215−224.
[11] J.R. Gonzalez-Velasco, A. Aranzabal, J.I. Gutierrez-Ortiz, R. Lopez-Fonseca, M.A. Gutierrez-Ortiz, Appl. Catal. B: Environ. 19 (1998) 189−197.
[12] P. Yang, S. Yang, Z. Shi, Z. Meng, R. Zhou, Appl. Catal. B: Environ. 162 (2015) 227−235.
[13] F. Bertinchamps, C. Poleunis, C. Grégoire, P. Eloy, P. Bertrand, E.M. Gaigneaux, Surf. Interface Anal. 40 (2008) 231−236.
[14] Q. Dai, S. Bai, H. Li, W. Liu, X. Wang, G. Lu, Appl. Catal. B: Environ. 168−169 (2015) 141−155.
[15] N. Blanch-Raga, M.D. Soriano, A.E. Palomares, P. Concepción, J. Martínez-Triguero, J.M.L. Nieto, Appl. Catal. B: Environ. 130−131 (2013) 36−43.
[16] J. González-Prior, R. López-Fonseca, J.I. Gutiérrez-Ortiz, B. de Rivas, Appl. Catal. B: Environ. 199 (2016) 384−393.
[17] M.D. Robayo, B. Beaman, B. Hughes, B. Delose, N. Orlovskaya, R.-H. Chen, Energy 76 (2014) 477−486.
[18] I.S. Yakovleva, L.A. Isupova, S.V. Tsybulya, A.V. Chernysh, N.N. Boldyreva, G.M. Alikina, V.A. Sadykov, J. Mater. Sci. 39 (2004) 5517−5521.
[19] Z. Zhang, Z. Jiang, W. Shangguan, Catal. Today 264 (2016) 270−278.
[20] L. Predoana, B. Malic, M. Kosec, M. Carata, M. Caldararu, M. Zaharescu, J. Eur. Ceram.Soc. 27 (2007) 4407−4411.
[21] H. Taguchi, S. Yamasaki, A. Itadani, M. Yosinaga, K. Hirota, Catal. Commun. 9 (2008) 1913−1915.
[22] N. Merino, B. Barbero, P. Grange, L. Cadus, J. Catal. 231 (2005) 232−244.
[23] L. Takacs, J. Mater. Sci. 39 (2004) 4987−4993.
[24] S. Laassiri, N. Bion, D. Duprez, S. Royer, H. Alamdari, Phys. Chem. Chem. Phys. 16 (2014) 4050.
[25] Y. Liu, H. Dai, J. Deng, L. Zhang, C.T. Au, Nanoscale 4 (2012) 2317.
[26] Y. Liu, H. Dai, Y. Du, J. Deng, L. Zhang, Z. Zhao, Appl. Catal. B: Environ. 119−120 (2012) 20−31.
[27] Y.X. Liu, H.X. Dai, J.G. Deng, X.W. Li, Y. Wang, H. Arandiyan, S.H. Xie, H.G. Yang, G.S. Guo, J. Catal. 305 (2013) 146−153.
[28] N. Li, A. Boréave, J.-P. Deloume, F. Gaillard, Solid State Ionics 179 (2008) 1396−1400.
[29] Z. Zhao, X. Lin, R. Jin, G. Wang, T. Muhammad, Appl. Catal. B: Environ. 115−116

(2012) 53–62.

[30] B. de Rivas, R. López-Fonseca, C. Jiménez-González, J.I. Gutiérrez-Ortiz, J. Catal. 281 (2011) 88–97.

[31] H. Arandiyan, H. Dai, J. Deng, Y. Liu, B. Bai, Y. Wang, X. Li, S. Xie, J. Li, J. Catal. 307 (2013) 327–339.

[32] Y. Wang, H. Arandiyan, J. Scott, M. Akia, H. Dai, J. Deng, K.-F. Aguey-Zinsou, R. Amal, ACS Catal. 6 (2016) 6935–6947.

[33] M. Zawadzki, J. Trawczyński, Catal. Today 176 (2011) 449–452.

[34] S. Royer, F. Bérubé, S. Kaliaguine, Appl. Catal. A: Gen. 282 (2005) 273–284.

[35] R. Ding, C. Li, L. Wang, R. Hu, Appl. Catal. A: Gen. 464–465 (2013) 261–268.

[36] J.M. Giraudon, A. Elhachimi, F. Wyrwalski, S. Siffert, A. Aboukaïs, J.F. Lamonier, G. Leclercq, Appl. Catal. B: Environ. 75 (2007) 157–166.

[37] Y.N. Cao, L.J. Shen, X.L. Hu, Z.J. Du, L.L. Jiang, Chem. Eng. J. 306 (2016) 124–130.

[38] H. Pan, Y. Guo, H.T. Bi, Chem. Eng. J. 280 (2015) 66–73.

[39] S. Zhan, M. Qiu, S. Yang, D. Zhu, H. Yu, Y. Li, J. Mater. Chem. A. 2 (2014) 20486–20493.

[40] Z. Li, J. Wu, J. Yu, D. Han, L. Wu, J. Li, J. Mol. Catal. A: Chem. 424 (2016) 384–392.

[41] T. Cai, H. Huang, W. Deng, Q. Dai, W. Liu, X. Wang, Appl. Catal. B: Environ. 166–167 (2015) 393–405.

[42] K. Ji, H. Dai, J. Deng, L. Song, B. Gao, Y. Wang, X. Li, Appl. Catal. B: Environ. 129 (2013) 539–548.

[43] Z. Zhao, H. Dai, J. Deng, Y. Du, Y. Liu, L. Zhang, Microporous Mesoporous Mater. 163 (2012) 131–139.

[44] L. Bai, F. Wyrwalski, M. Safariamin, R. Bleta, J.-F. Lamonier, C. Przybylski, E. Monflier, A. Ponchel, J. Catal. 341 (2016) 191–204.

[45] Y. Li, Y. Wan, Y. Li, S. Zhan, Q. Guan, Y. Tian, ACS Appl. Mater. Interfaces 8 (2016) 5224–5233.

[46] H. Huang, Y. Gu, J. Zhao, X. Wang, J. Catal. 326 (2015) 54–68.

[47] J.G. Deng, H.X. Dai, H.Y. Jiang, L. Zhang, G.Z. Wang, H. He, C.T. Au, Environ. Sci. Technol. 44 (2010) 2618–2623.

[48] S. Royer, D. Duprez, F. Can, X. Courtois, C. Batiot-Dupeyrat, S. Laassiri, H. Alamdari, Chem. Rev. 114 (2014) 10292–10368.

[49] J. Zhu, H. Li, L. Zhong, P. Xiao, X. Xu, X. Yang, Z. Zhao, J. Li, ACS Catal. 4 (2014) 2917–2940.

[50] C. Zhang, C. Wang, W. Zhan, Y. Guo, Y. Guo, G. Lu, A. Baylet, A. Giroir-Fendler, Appl. Catal. B: Environ. 129 (2013) 509–516.

[51] P. Yang, S. Yang, Z. Shi, Z. Meng, R. Zhou, Appl. Catal. B: Environ. 162 (2015) 227–235.

[52] Z. Boukha, J. González-Prior, Bd. Rivas, J.R. González-Velasco, R. López-Fonseca, J.I. Gutiérrez-Ortiz, Appl. Catal. B: Environ. 190 (2016) 125–136.

[53] S. Bai, Q. Dai, X. Chu, X. Wang, RSC Adv. 6 (2016) 52564–52574.

[54] P.S. Chintawar, H.L. Greene, J. Catal. 165 (1997) 12–21.

[55] W. Wang, Q. Zhu, Q. Dai, X. Wang, Chem. Eng. J. 307 (2017) 1037–1046.

[56] C. He, Y. Yu, J. Shi, Q. Shen, J. Chen, H. Liu, Mater. Chem. Phys. 157 (2015) 87–100.

[57] J. Lichtenberger, J. Catal. 223 (2004) 296–308.

[58] Y. Liu, W.C. Wu, Y.J. Guan, P.L. Ying, C. Li, Langmuir 18 (2002) 6229–6232.

[59] P.S. Chintawar, H.L. Greene, Appl. Catal. B: Environ. 13 (1997) 81–92.

[60] Q. Huang, X. Xue, R. Zhou, J. Mol. Catal. A: Chem. 344 (2011) 74–82.

[61] Q. Huang, X. Xue, R. Zhou, J. Mol. Catal. A: Chem. 331 (2010) 130–136.